https://doi.org/10.1016/j.jcsr.2023.108335

Experimental and numerical exploration for the design of swift-constructed demountable blind bolts

Xiao-Zhou Han [a], Chen Wang [a,*], and Tak-Ming Chan [a,b]

[a] Department of Civil and Environmental Engineering, The Hong Kong Polytechnic University, Hung Hom, Hong Kong, China

[b] Chinese National Engineering Research Centre for Steel Construction (Hong Kong Branch), The Hong Kong Polytechnic University, Hung Hom, Hong Kong, China

*Corresponding author: chen.wang5@mail.mcgill.ca

Abstract

In this study, a new type of blind bolt that combines high tensile resistance and stiffness with easy and fast installation and demounting capabilities is proposed, named Swift-Constructed Demountable Blind Bolt (SCDBB). The components, intended working mechanism, and fabrication process are first introduced. Geometric constraints of critical components are then derived based on the desired behaviour. To study the performance of SCDBBs under tensile loading and their behaviour during the installation process, 9 experimental tests were conducted. Two failure modes, namely, bolt shank fracture and buckling of the expansion nut blades, were revealed when subjected to maximum tensile loading. Subsequently, finite element (FE) models were developed and validated by comparing the numerical results with the experimental data. To further explore the impact of key design parameters on the behaviour of the bolts under tensile loading and performance during installation, parametric studies consisting of 106 FE models were conducted for bolts of three sizes with variations in four key design parameters. The findings indicate that the failure modes under maximum tensile loading and maximum installation force are sensitive to the length, thickness, and gap of the elastic expansion nut. The optimised ranges for each design parameter were identified to prevent undesirable blade buckling.

Keywords: Blind bolt, Demountable, Fast installation, Fast removal, High-strength bolt

1.Introduction

In recent decades, researchers have faced the challenge of no access to the inside of hollow section columns for nut installation. Various solutions have been put forward, such as Flowdrill drilling system, stud welding, and nuts pre-welded into the hollow section wall [1]. However, these methods require additional on-site work and result in increased costs. To address this issue, blind bolts have been developed and Fig. 1 provides an overview of several existing blind bolt products, including Hollo-bolt [2], Thin Wall Bolt [3], Oneside Bolt [4], Oneside Hi-shear Bolt [5], Huck Blind Fasteners [6], Blind Bolt [7], Heavy Duty Bolt [8], and Juck Nut [9]. Regarding the Hollo-bolt (Fig. 1a and Fig. 2b), it has been successfully used in the construction industry for a long time and extensively researched by multiple experts [10–16]. Additionally, a modified version, the Extended Hollo-bolt, designed for concrete-filled steel tubular column connections, has also been proposed and studied by several research groups [17–20]. However, although this bolt performs well in shear connections, it lacks the necessary clamping force to prevent axial deformation at high tensile loads [21].

To address this issue, Barnett et al. [22] modified the Hollo-bolt and developed the Reverse Mechanism Hollo-bolt (RMH) (Fig. 2a), in which the expanding part is inverted to achieve comparable tensile stiffness and strength to a standard high-strength bolt. The Thin Wall Bolt (Fig. 1b) is a commercially available product that incorporates the design of the RMH. Tensile behaviour comparisons between the Hollo- bolt and RMH were conducted by Barnett et al. [22] (Fig. 2). The RMH exhibited significantly higher tensile stiffness than the Hollo-bolt. However, its tensile resistance is affected by the mechanism with reversed expanding sleeve, leading to lower tensile capacity.

Tizani & Ridley-Ellis [21] further studied the application of RMH in unfilled rectangular hollow section connections, focusing on connection tension behaviour under tube wall yielding failure mode. The findings revealed that connections made with the RMH are stiffer, have better tensile resistance, and exhibit greater ductility compared to those made with the Hollo-bolt. The mechanical mechanisms of these bolts in connection become more critical than the bolt tensile resistance itself when the tube wall failure mode governs the connection behaviour.

However, these findings are limited to specific practical scenarios. If the application involves a thick tube wall and weaker bolts, the performance of the RMH may not exceed that of the Hollo-bolt. It indicates that the initial attempt to develop the RMH did not fully achieve the desired target at the component level. Additionally, the current commercial product Thin Wall Bolt (Fig. 1b), which adopts the concept of the RMH, is only available in sizes up to M8. Thus, there is a need to develop a novel bolt with a similar mechanism to the RMH while achieving better tensile strength and larger bolt sizes.

Another widely used blind bolt is the Oneside Bolt (Fig. 1c), and its modified version called Oneside Hi-shear Bolt (Fig. 1d) is also available. Additionally, there are other popular blind bolt products from different countries (Fig. 1e to Fig. 1h). However, some of these blind bolts cannot be easily removed without machine cutting after installation. While some products allow for demountable structures by leaving certain components inside the tube during removal, the speed of installation and removal could be further improved.

Fig. 1. Overview of common commercially available blind bolts with brand names in the bracket.

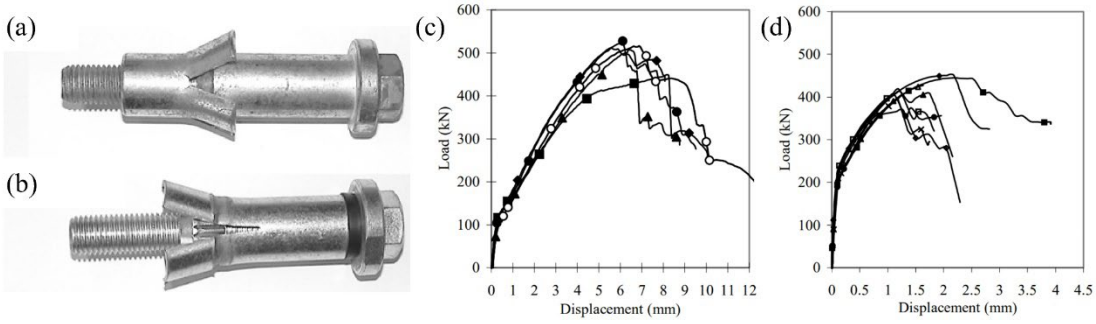

Fig. 2. (a) Reverse Mechanism Hollo-bolt (RMH) and (b) Hollo-bolt [21]; Tensile behaviour comparison between Hollo-bolt (c) and RMH (d) [22].

Through extensive analysis of existing blind bolts, it becomes evident that there is a distinct demand for a blind bolt that combines high tensile resistance and stiffness with easy and fast installation/demounting capabilities. In response to this demand, this study proposes a new type of demountable blind bolt, named Swift-Constructed Demountable Blind Bolt (SCDBB). The components and intended working mechanism of SCDBB are first introduced. Geometric constraints of the critical components are then derived based on the desired behaviour. Subsequently, experimental tests were conducted to analyse the behaviour of SCDBBs when subjected to tensile loading and performance during the installation process. Next, numerical finite element (FE) models were developed and validated through comparison between the numerical and test results. To further explore the impact of key design parameters on the behaviour of the bolts under tensile loading and their performance during the installation process, parametric studies consisting of 106 FE models were conducted for bolts of three sizes with variations in four key design parameters. The insights gained from this parametric study were used to optimise the design of SCDBBs.

2.The swift-constructed demountable blind bolt (SCDBB)

With the motivation for a blind bolt that combines high tensile resistance and stiffness with easy and fast installation and demounting capabilities, a novel swift-constructed demountable blind bolt (SCDBB) is proposed [23]. In this section, the components, the installation and removal processes, the working mechanism and the fabrication method will be elaborated.

2.1. Components

The SCDBB consists of four components, namely, the bolt shank, nut, sleeve, and elastic expansion nut (EEN), as illustrated in Fig. 3. The geometric parameters of EEN

are illustrated in Fig. 4. The EEN consists of two parts: the blades and the ring nut. The blades are made by cutting a hollow conical frustum with a constant thickness (i.e., the thickness of the blades, denoted by t). The smaller base of the conical frustum is connected with the ring nut. The difference between the radius of the smaller base of the conical frustum and the radius of the larger base is referred to as the gap of the blades and denoted by g. With the existence of the gap, the diameter of the blades is intended to be larger than that of the bolt hole. Threads that match that of the bolt shank exist inside the nut and the EEN.

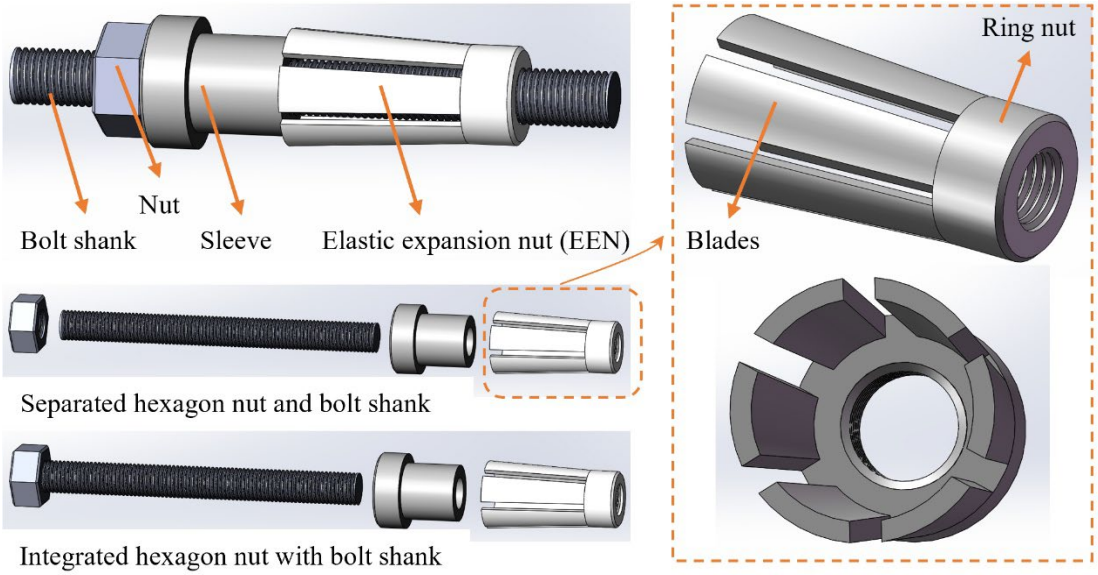

Fig. 3. Components of the swift-constructed demountable blind bolt (SCDBB).

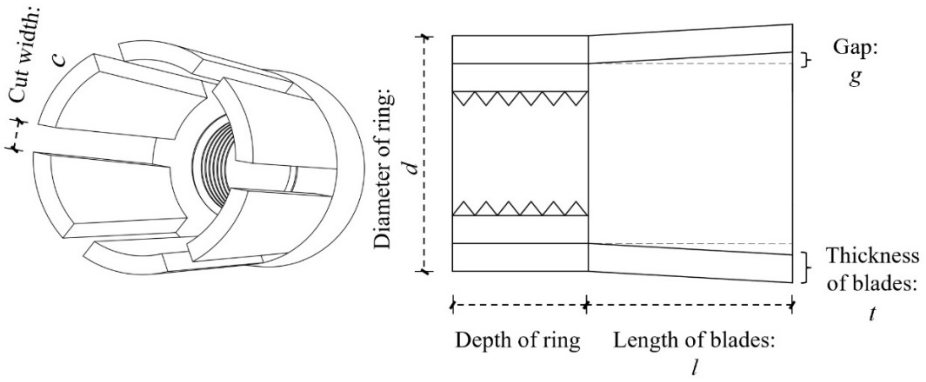

Fig. 4. Geometric parameters of the elastic expansion nut (EEN).

2.2. Installation and removal process

The step-by-step installation and removal processes are illustrated in Fig. 5. Regarding the installation process, firstly, the EEN can be assembled on the bolt shank like a traditional bolt and nut. The EEN will then be pushed through the bolt hole. During this process, the blades will be compressed as one side of it has a larger diameter than that of the bolt hole. It is noted that due to the contact force between the EEN and the bolt hole, this installation process has to overcome the frictional forces. Once the entire EEN passes the bolt hole, the blades will expand immediately back to their initial shapes. Subsequently, the sleeve will be installed. After that, the nut will be installed and tightened to complete the whole installation process.

Alternatively, the multi-step installation process mentioned above can be further simplified by assembling the whole bolt in advance, and then just pushing it into the hole as presented by Fig. 5. The length of part of the sleeve that will be inserted into the bolt hole can be set as the thickness of the connected plates. Once the bolt stopped by the outside part of sleeve indicating the bolt is pushed to the right position, the outside nut can be tightened to complete the installation.

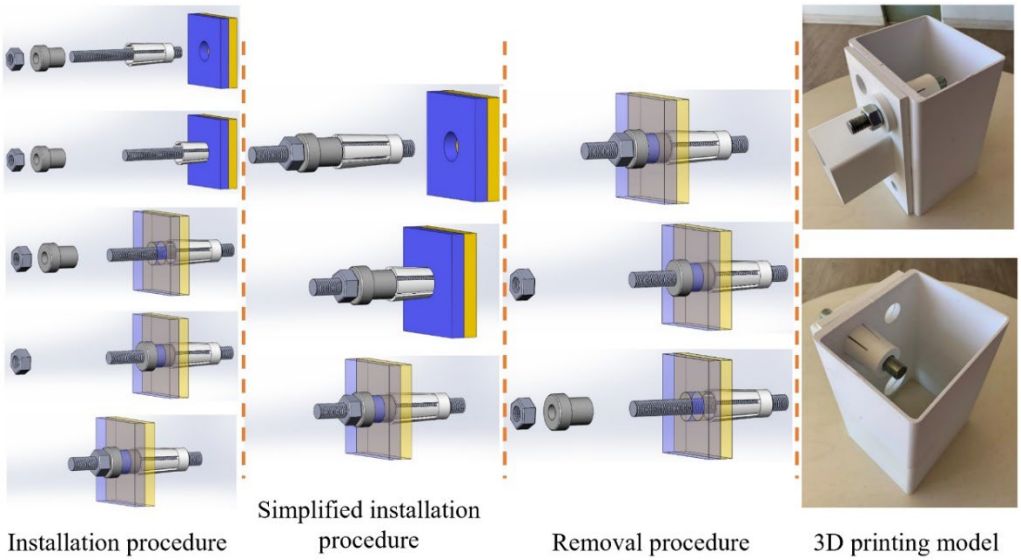

Fig. 5. Step-by-step installation and removal processes.

As mentioned above, it should be noted that a force is required to push the EEN through the bolt hole, and the range of this force should be reasonable to guarantee operability. Several installation force tests have been conducted in this study to investigate the required maximum force. In another comprehensive experimental investigation of SCDBB performed by the authors [24], a large amount of SCDBB specimens were fabricated according to the dimensions recommended by this study. Over 50 installation force tests of EEN were carried out to further check this installation force. The corresponding results showed that the installation forces were below 1 kN (most around 0.4 to 0.8 kN) and could be accomplished by a single site worker using a hammer. However, it should be noted that the installation forces are not negligible. An auxiliary installation tool for the SCDBB has also been invented by authors [25] to help workers easily apply the installation force and offset the reaction force during the installation process, as illustrated in Fig. 6. Workers can conveniently operate the auxiliary installation tool using a single hand to hold the hand gripping arms. By gripping the handle to increase the opening angle of the end of the retractable clamping arm, the hook of the retractable clamping arm makes contact with the back of the column, allowing the clamping arm to securely clamp the column via the elastic force of the spring. The position of the load transfer head can be adjusted by the slider, aligning it with the position of the SCDBB. Subsequently, by rotating the hex bolt head with a wrench, the load transfer head moves towards the column, resulting in the application of an axial installation force in the axial direction of the SCDBB. It is important to note that the hook of this tool effectively counteracts the reaction force generated during the insertion of the SCDBB into the bolt hole. Once the EEN of SCDBB passes through the bolt hole, the sleeve of SCDBB prevents further movement. Finally, the auxiliary

installation tool can be removed, and a torque wrench can be used to apply the required preloading by further tightening the SCDBB.

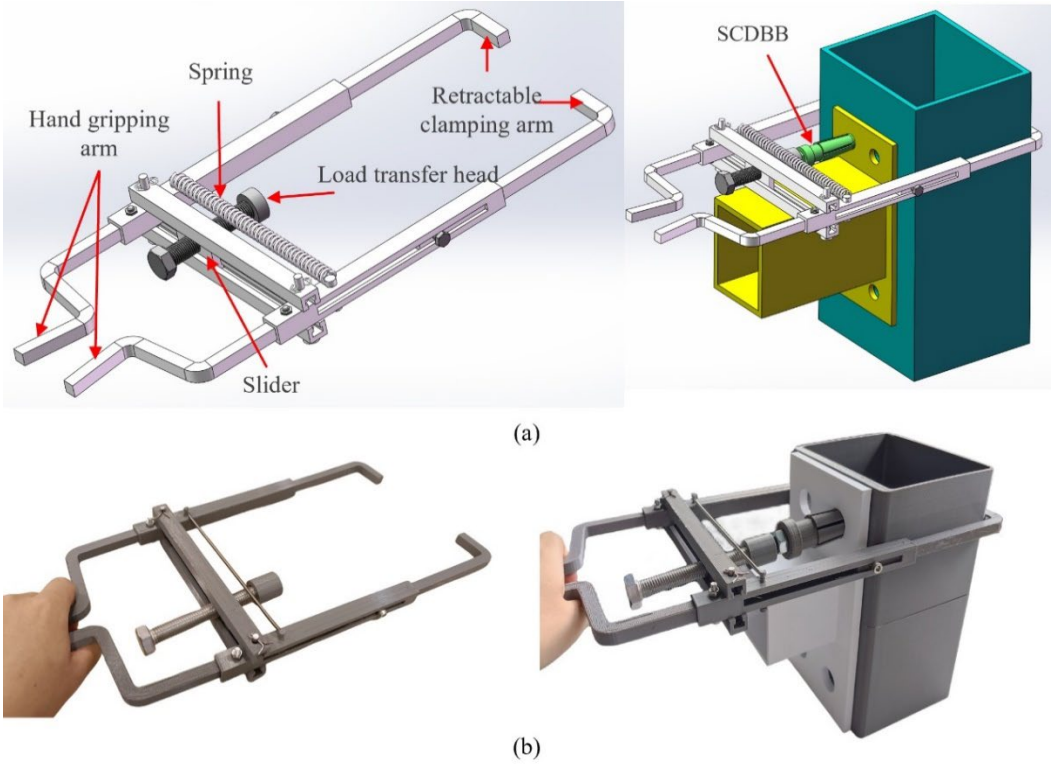

Fig. 6. Auxiliary installation tool for the SCDBB: (a) schematic diagram, (b) 3D printing prototype.

Regarding the removal of SCDBBs, the whole process can be completed in a fast manner by simply loosening the outside nut first, and then pulling and rotating the bolt shank to let the EEN separating from the shank and falling into the inner space of column. As such, except for the EEN, all other components of this bolt (the nut, shank and sleeve) can be retrieved and reused in the future. Such installation and removal processes have been validated through the 3D printing model before real fabrication.

2.3. Working mechanism and desired behaviour

As the outer diameter of the blades of EEN is larger than that of the bolt hole, tightening the nut causes the EEN to move outward from the column inside. Consequently, the

blades can firmly grasp the inner surface of column wall, creating a robust clamping force that effectively connects the components. This clamping mechanism is designed to provide the necessary resistance to tensile forces, while the bolt shank with sleeve serve together to offer the essential shear resistance.

To ensure the desired functionality of this working mechanism, two performance objectives shall be met during installation and under maximum tensile loads:

(1) It is crucial for the blades to return to their initial shapes after installation and grip the inner wall when the nut is tightened externally. To achieve this, the blades shall remain elastic throughout the installation process, especially when they are compressed to pass through the bolt hole.

(2) Under maximum tensile loads, it is preferable for the clamping mechanism to be maintained while the bolt shank fails through fracture. The blades should remain elastic, avoiding other failure modes such as buckling.

2.4. Fabrication of the elastic expansion nut

In this study, the bolt shanks are Grade 8.8 (with minimum nominal ultimate strength of 800 MPa and yield strength of 640 MPa), which are available on the commercial market. For the steel material of the EEN, a higher grade of 10.9 is intended, with the intention of securing the higher strength of the EEN than the bolt shank. To achieve the intended strength, the suitable raw material was carefully selected, and an appropriate heat treatment process was adopted. Li [26] introduced the raw material selection of blind bolt based on the China steel products with relevant Chinese steel material standards. In addition, through studying the material selection of high-strength bolts mentioned by researchers [27,28], 40Cr alloy structural steel was selected. The heat

treatment process recommended by the current alloy structural steel standard GB/T 3077 [29] was adopted.

To verify if the properties of the steel after heat treatment have met the intended requirement, various tests, including strength test, hardness test, and metallographic examination were conducted by authors [30]. Results of strength tests are illustrated in Fig. 7. It can be found that the yield strength and ultimate strength of 40Cr steel can be significantly improved through the selected heat treatment procedure. After the heat treatment, the yield strength increased to 996 MPa, and the ultimate strength raised to 1158 MPa, which meets the strength requirement for Grade 10.9. Moreover, the hardness test results reveal that the hardness of the EEN made of 40Cr steel with heat treatment is HRC 35.8, which meets the requirements for Grade 10.9 bolts specified in GB/T 3098.1 [31] and ISO 898-1 [32]. The results of the metallographic examination are presented in Fig. 8. As shown, the microstructure of the 40Cr raw material features ferrite and pearlite, which is typical of low-carbon steel with relatively low strength. While tempered martensite can be easily recognized in the steel with heat treatment which is typical of high- strength steel.

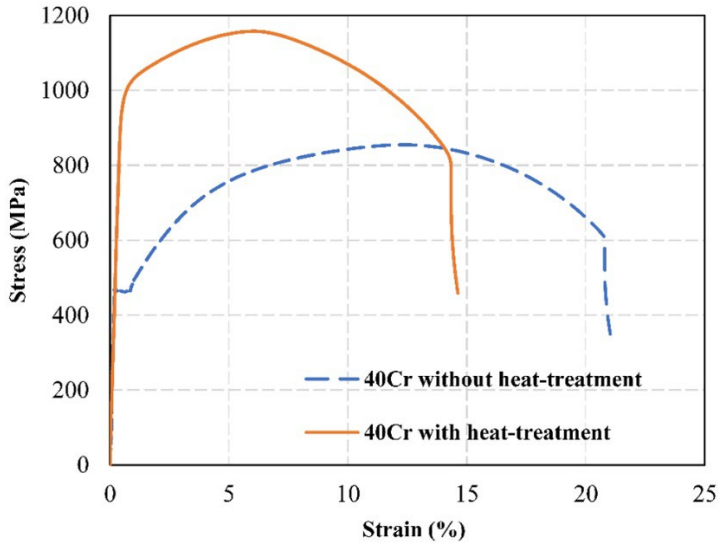

Fig. 7. Stress-strain curves of 40Cr steel with and without heat treatment [30].

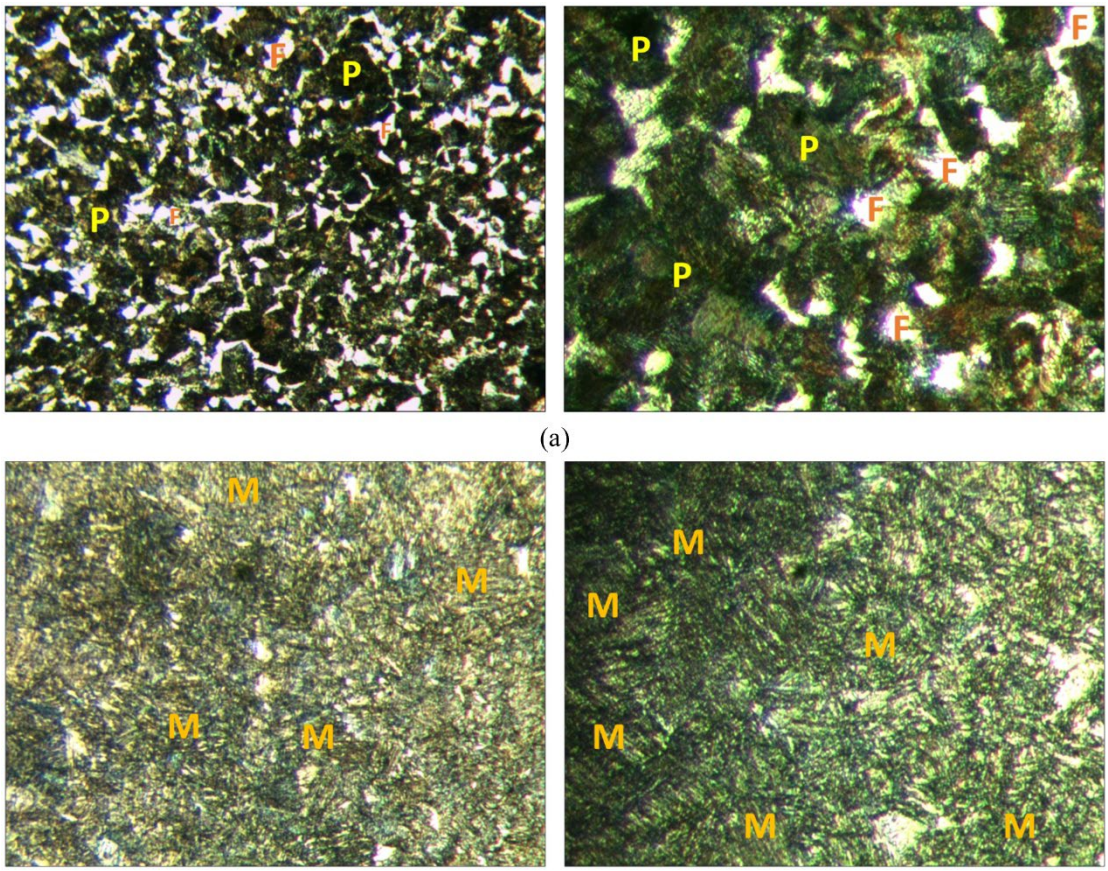

Fig. 8.Optical microstructure of 40Cr steel: (a) without heat treatment, (b) with adopted heat treatment (Note: ‘P', ‘F', ‘M' stand for pearlite, ferrite, martensite, respectively) [30].

Fig. 9 highlights the major steps and status involved in the fabrication process of EENs. Firstly, the components were machined from raw steel bars by using the computer numerical control (CNC) fabrication approach, ensuring precise geometric dimensions. Subsequently, heat treatment was carried out to attain the desired material properties, followed by the application of CNC fine finishing techniques. Lastly, the fabrication process was completed by obtaining slots between the blades through wire cutting. Although the cost is relatively high for fabrication of test specimens, it is expected to be considerably reduced for mass production in the future. Moreover, cast-in fabrication method may also be a suitable choice for mass production of this bolt in the future.

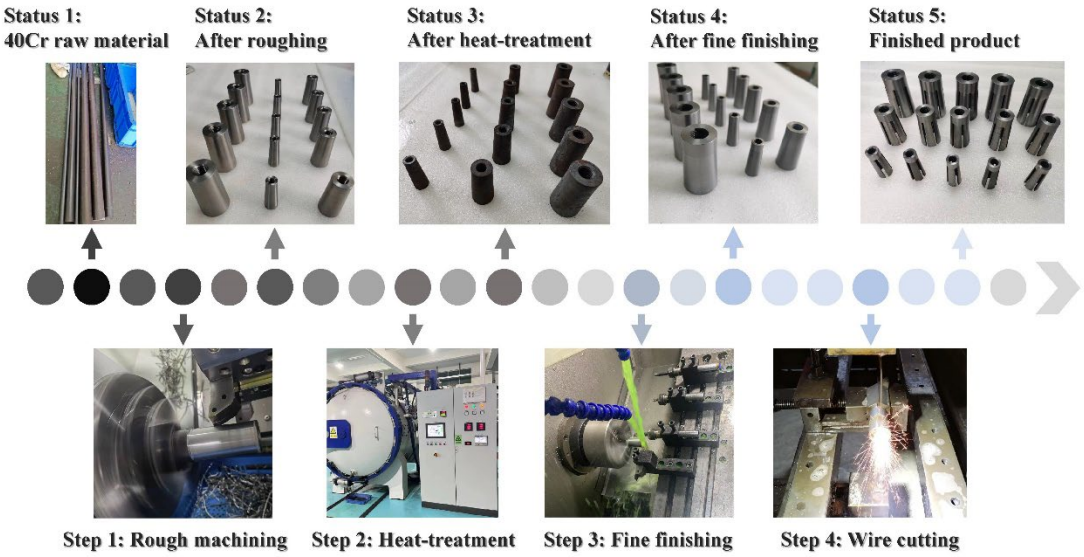

Fig. 9. Fabrication process of EENs.

3.Preliminary geometric dimensioning

This section serves as a preliminary determination of the dimensions for the proposed SCDBBs, providing a starting point for further study and design optimisation in subsequent sections. Initially, the sizes of bolt shanks, threads, and nuts can be assumed to be the same as those of corresponding conventional bolts according to EN 14399–3: 2015 [33]. The study focused on three specific sizes: M8, M12, and M16. Similarly, the ring nut of the EEN serves a similar function to the nut, so similar dimensions were adopted. Specifically, for M8, M12, and M16, the outer diameter of the ring nut was set at 12.6 mm, 23 mm, and 32 mm, respectively, with a depth of 8 mm, 11 mm, and 15 mm. Regarding the sleeve, the section to be inserted into the bolt hole shares the same outer diameter as the ring nut of the EEN. The section responsible for providing the clamping force was designed with a larger diameter than the width across corners of nut. Specifically, for the M8, M12, and M16 SCDBBs, the corresponding dimensions of this section in sleeves are 18 mm, 29 mm, and 39 mm, respectively. For the blades of the EEN, the preliminary derivation of dimension constraints will be based on the

desired behaviour, which will be further elaborated in subsequent sections. The corresponding bolt hole diameters for M8, M12, and M16 SCDBBs are 13 mm, 23.6 mm, and 32.8 mm, respectively.

3.1.Cut width of the blades (c)

The compression of the EEN blades is necessary for them to pass through the bolt hole. To ensure smooth insertion, it is crucial to avoid any conflicts between the blades when they are compressed and confined within the bolt hole. By considering the minimal difference between the bolt hole radius and the outer radius of the blade end face, this requirement can be further described as ensuring that the total length of the outer sides of the blades remains smaller than the circumference of the bolt hole. Mathematically, this can be expressed as:

$$2\pi\left(\frac{d_{ring}}{2}+g\right)-n_c c \leq \pi d_{hole} \quad (1)$$

where d_{ring} is the outer diameter of the ring nut of the EEN, g is the gap size, n_c =number of cuts (4 for M8; 6 for M12 and M16 in this study), and d_{hole} is the diameter of the bolt hole.

3.2. Thickness of the blades (t)

As discussed in Section 2.3, the desired failure mode for SCDBBs under maximum tensile loading is the fracture of the bolt shank while the EEN remains elastic. In order to achieve this, it is necessary for the yielding strength of the blades to exceed the ultimate strength of the bolt shank. Mathematically, this can be expressed as:

$$A_{blades} f_{y,EEN} > A_{shank} f_{u,shank} \quad (2)$$

where A_{blades} = the cross-sectional area of blades, A_{shank} = the threaded cross-sectional area of bolt shank, $f_{y,EEN}$ = yield strength of the steel of EEN, $f_{u,shank}$ = the ultimate strength of the steel of bolt shank. The cross-sectional area of the blades can be calculated as:

$$A_{blades} = \pi \left[\left(\frac{d}{2} \right)^2 - \left(\frac{d}{2} - t \right)^2 \right] - n_c c t \qquad (3)$$

Considering the constraint provided in Eq. (3), the minimal thickness of the blades can be determined once the cut width and number of cuts have been established.

3.3. Gap of the blades (g)

To achieve the desired behaviour, it is crucial for the blades to return to their original shapes after passing through the bolt hole to ensure proper contact with the connected component. To fulfil this requirement, one extreme condition is that when the EEN is compressed and confined in the bolt hole, the stress of the extreme fibre at the blade root just reaches the yield strength, or equally, the bending moment at the blade root just reaches the yield moment of the section. By solving this problem, the upper limit of the gap of the blades can be determined. And it can be studied by treating the blade as a beam which is fixed on the one side and loaded in a direction perpendicular to the bolt hole surface on the other side, as illustrated in Fig. 10. Since the structure and loading have axial symmetry, the problem can be simplified as a plane problem with a unity depth.

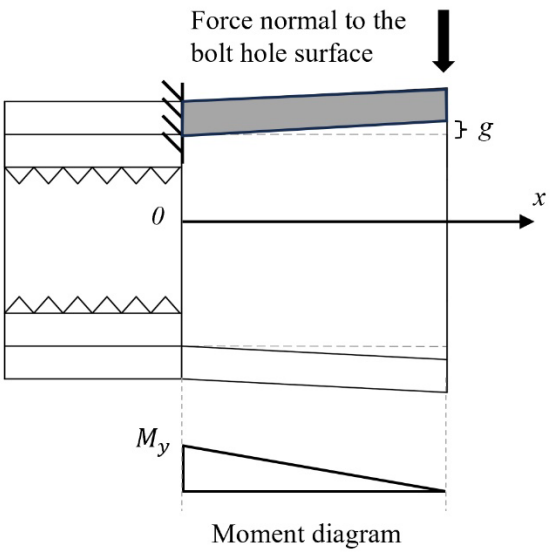

Fig. 10. Simplified beam model for blades under bending.

When the bending moment at the fixed end section equals the yield bending moment of section (denoted by M_y), the bending moment along the x-axis (as shown in Fig. 10) can be expressed as:

$$M(x) = M_y(1 - \frac{x}{l}) \tag{4}$$

Consequently, the curvature ϕ can be represented as a function of the moment:

$$\phi(\mathrm{x}) = \frac{M(x)}{EI} = \frac{M_y}{EI}(1 - \frac{x}{l}) \tag{5}$$

Subsequently, the curvature ϕ can be integrated once to find the rotation (or slope) θ as a function of the location along the beam x, and twice to find the deflection Δ as a function of x,

$$\theta(x) = \int \phi(\mathrm{x})dx = \frac{M_y}{EI}(x - \frac{x^2}{2l} + C) \tag{6}$$

$$\Delta(x) = \iint \theta(\mathrm{x})dx = \frac{M_y}{EI}(\frac{x^2}{2} - \frac{x^3}{6l} + Cx + D) \tag{7}$$

Considering that the rotation and deflection at the fixed end are both zero that is, $\theta(0)$=0, and $\Delta(0)$=0, the constants in Eqs. (6) and (7), can be solved as C=D=0.

In the extreme condition, the deflection at the non-fixed end of the blades corresponds to the maximum gap, that is,

$$g < \Delta(l) = \frac{M_y}{EI}\frac{l^2}{3} \tag{8}$$

Since the yield moment can be calculated as M_y=$2f_{y,EEN}I/t$ by assuming the stress of the section's extreme fiber reaches the yield strength, Eq. (8) can be further simplified as:

$$g < \frac{2f_{y,EEN}l^2}{3Et} \tag{9}$$

3.4.Length of the blades (l)

Under tensile loading, the EEN blades experience primarily axial compression. One potential failure mode of the blades is buckling, which is undesirable as it completely alters the force resisting mechanism and can lead to sudden loss of resistance. The buckling resistance of the blades can be estimated by treating them as columns. Due to the axial symmetry of the blades and the loading, the problem can be simplified as a plane problem with a unity depth, as shown in Fig. 11.

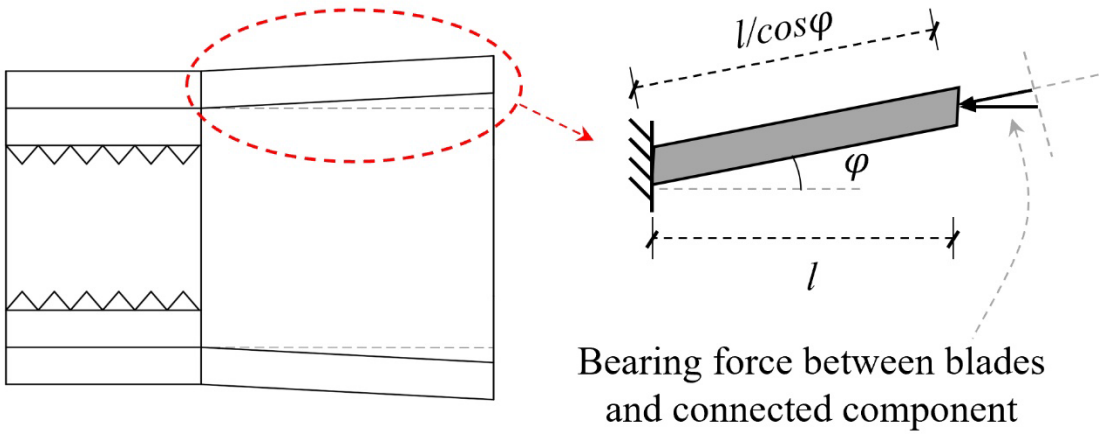

Fig. 11.Simplified column model for blades under compression.

For these blades, the critical Euler stress in the axial direction can be calculated as

$$\sigma_{cr} = \frac{\pi^2 EI}{(Kl/cos\varphi)^2 A} = \frac{\pi^2 t^2 E}{12(Kl/cos\varphi)^2} \quad (10)$$

To prevent premature buckling of the blades before the bolt shank fractures, it is necessary to ensure that the resistance of blades is greater than the ultimate resistance of bolt shank, given by

$$A_{shank} f_{u,shank} cos\varphi \leq \sigma_{cr} A_{blades} \quad (11)$$

This can be further expressed as

$$(Kl)^2 \leq \frac{\pi^2 t^2 E A_{blades} cos\varphi}{12 A_{shank} f_{u,shank}} \quad (12)$$

It is important to note that *K* represents the column effective length factor to account for different boundary conditions. For the blades of EEN, one end is fixed with the ring nut, which is considered fixed. The other end is almost rotation-free, but due to the presence of friction force between the blades and the connected component, it lies between translation-free (with a corresponding *K* factor of 1.0) and translation- fixed (with a corresponding *K* factor of 0.7). In this study, a value of 0.85 was used to estimate the buckling resistance, which was verified to be reasonable and conservative by the test results presented in Section 4.3.

4.Experimental tests

4.1.Test specimens and material properties

This section presents the results of the experimental tests conducted to investigate the behaviour of the proposed SCDBBs. Specifically, five tests as shown in Fig. 12 were performed to analyse the behaviour under tensile loading, while another four tests focused on studying the behaviour during installation. On the one hand, regarding the tensile loading tests, the main objectives were to assess the ultimate resistance and identify the failure modes. On the other hand, the installation tests aimed to determine

the maximum push force and potential plasticity in blades of the EEN during the installation process. Table 1 provides details of the nine experimental specimens used in these tests. The labels of the specimens indicate the bolt size, with letters ‘c’, ‘t’, ‘g’, and ‘l’, denoting the cut width, thickness, gap, and length of the blades, respectively. The number preceding each letter corresponds to the geometric dimension in millimetres. For example, the specimen labelled ‘M8 2.5c 2.3t 1.5g 37l’ refers to a specimen with an M8 bolt shank, while the cut width, thickness, gap, and length of the blades are 2.5 mm, 2.3 mm, 1.5 mm, and 37 mm, respectively.

Fig. 12.Photo of test specimens.

Table 1 Test specimen information

Test type	Specimen Label	Bolt shank grade	Bolt shank diameter (mm)	c (mm)	t (mm)	g (mm)	l (mm)	Diameter of EEN ring (mm)	Depth of EEN ring (mm)
Tensile loading test	M8 2c 2.3t 1.7g 20l	10.9	8	2.0	2.3	1.7	20	12.6	8
	M8 2.5c 2.3t 1.5g 37l	10.9	8	2.5	2.3	1.5	37	12.6	8
	M8 2.7c 2.2t 1.8g 37l	10.9	8	2.7	2.2	1.8	37	16.0	8
	M12 3c 2t 2g 39l	8.8	12	3.0	2.0	2.0	39	21.0	11
	M16 2.5c 2.2t 2g 45l	8.8	16	2.5	2.2	2.0	45	32.0	15
Installation test	M8 2.5c 2.3t 1.5g 37l	-	8	2.5	2.3	1.5	37	12.6	8
	M8 2.7c 2.2t 1.8g 37l	-	8	2.7	2.2	1.8	37	16.0	8
	M12 3c 2t 2g 39l	-	12	3.0	2.0	2.0	39	21.0	11
	M16 2.5c 2.2t 2g 45l	-	16	2.5	2.2	2.0	45	32.0	15

It should be noted that the dimensions of the test specimens did not strictly adhere to the geometric constraints outlined in Section 3. This deviation was intentional in order to expose different failure modes and validate the numerical models described in subsequent sections. In the case of M8 specimens, Grade 10.9 bolt shanks were utilized to facilitate comparison with RMH, as only Grade 10.9 RMHs are currently available in the market, the corresponding results have been reported by authors [30]. The material properties of each component of the test specimens were determined through tension coupon tests. Circular coupons were fabricated from steel bars used to construct the test specimen components. However, due to the small size of the M8 bolt shank, it was not feasible to fabricate a tension coupon for the Grade 10.9 bolt shank. The material properties obtained from the different parts of the test specimens are provided in Table 2.

Table 1 Measured material properties

Component		Circular Coupons				
		E	$f_{y,c}$	$f_{u,c}$	$\varepsilon_{u,c}$	$\varepsilon_{f,c}$
		GPa	MPa	MPa	%	%
Grade 8.8 Bolt Shank	Coupon 1	208	946	1012	4.39	14.22
	Coupon 2	209	885	957	4.57	14.35
EEN	Coupon 1	211	996	1158	6.11	14.33
	Coupon 2	210	992	1149	5.24	13.30
Sleeve	Coupon 1	216	462	853	12.36	20.79
	Coupon 2	211	473	856	10.63	19.27

Note: Presented are true stress/strain values, with $\varepsilon_{u,c}$ and $\varepsilon_{f,c}$ referring to strains at ultimate stress and at fracture of coupons, respectively.

4.2.Test set-up and test programme

The experimental tests were carried out using an MTS 600 kN hydraulic tension machine. A specially designed test rig, depicted in Fig. 13, was utilized. The green plates in Fig. 13 represent the two components that will be joined together by the SCDBB. It should be noted that the thin green plates were for M8 specimens only to convenient the comparison with RMH, while thick green plates were used for M12/M16 specimens to ensure the test rig is rigid. For each test specimen, the plates with the corresponding bolt holes were fixed in place.

In the case of the tensile loading tests, two rods at the ends of the test rig were clamped to the upper and lower grips of the tension machine, and an axial load was applied, as shown in Fig. 14(a). Throughout the tests, the applied load and the displacement of the machine grips were constantly monitored and recorded. First, a preload of approximately 10% of the estimated bolt shank resistance was applied to prevent any slippage and verify the accuracy of the equipment. After the preloading stage,

displacement-controlled loading was implemented with a rate of 0.1 mm/min until failure occurred.

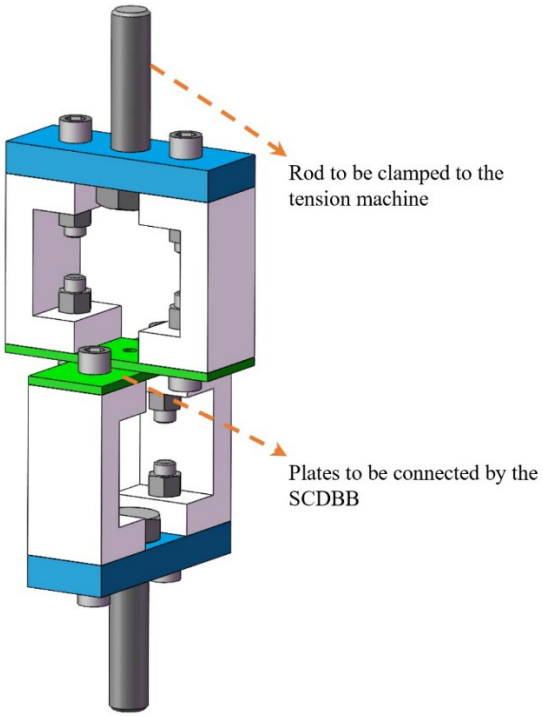

Fig. 13. Schematic of the test rig.

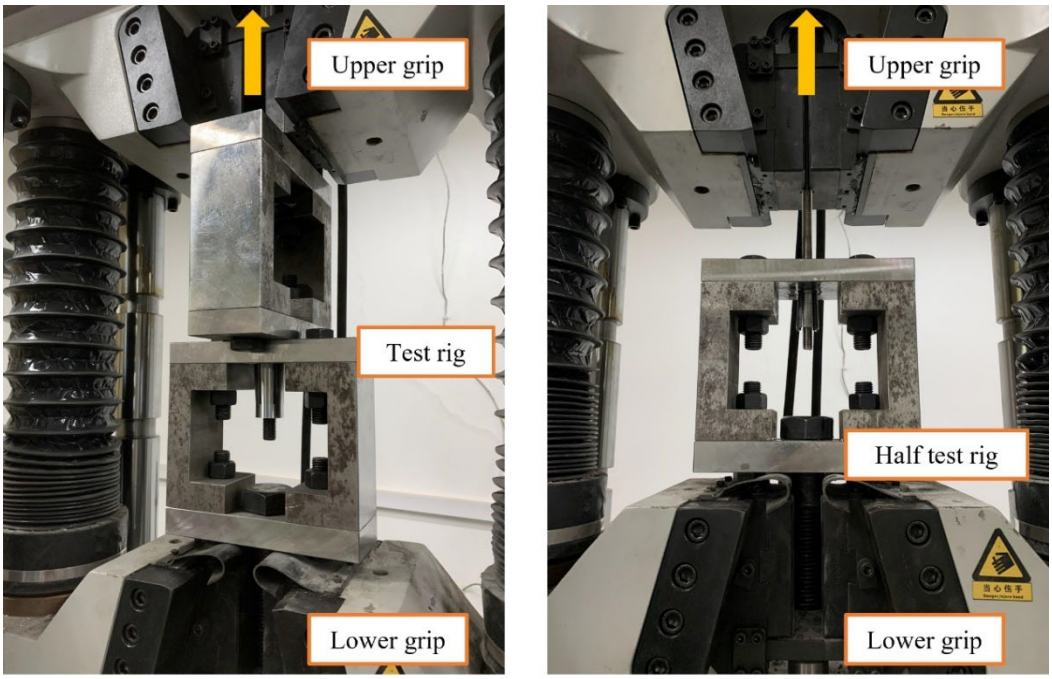

Fig. 14. Test setup photos: (a) for ultimate resistance, (b) for installation force.

For the installation tests, only the lower part of the test rig was employed and clamped to the lower grip of the tension machine, as shown in Fig. 14(b). In order to simulate the installation process, a long bolt shank along with the corresponding EEN was used. Initially, the EEN was positioned below the connected plate. The opposite end of the bolt shank was fastened to the upper grip of the tension machine. The upper grip applied an axial load to draw the EEN through the bolt hole. The applied load was continuously monitored and collected during the test. As it was challenging to affix strain gauges onto the EEN, the alteration in geometric dimensions before and after the installation process was analysed to assess the development of plasticity.

4.3.Test results and discussion

During the tensile loading tests, various failure modes were observed. In the case of the three M8 specimens, the bolt shanks fractured at the ultimate load, while no significant deformation was observed in the other components, as shown in Fig. 15(a)-(c). In the case of specimens M12 3c 2t 2g 39l and M16 2.5c 2.2t 2g 45l, buckling of the blades occurred at the ultimate load. For the development of the buckling, several blades buckled inward first, causing the EEN to incline towards the buckled blades and resulting in outward bending of the remaining blades. Fig. 15 (d) and (e) show the buckled blades of specimens M12 3c 2t 2g 39l and M16 2.5c 2.2t 2g 45l, respectively. Table 3 summarizes the results of the five tensile loading tests.

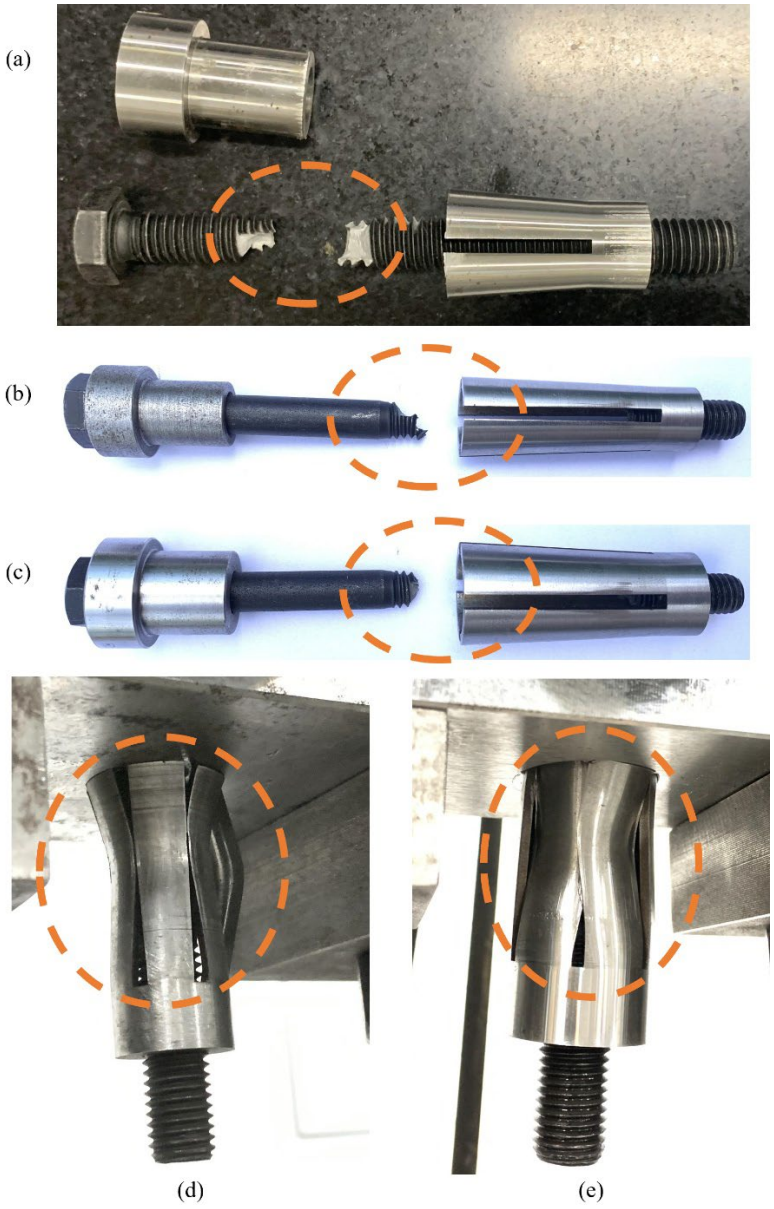

Fig. 15.Failure modes of: (a) M8 2c 2.3t 1.7g 20l, (b) M8 2.5c 2.3t 1.5g 37l, (c) M8 2.7c 2.2t 1.8g 37l, (d) M12 3c 2t 2g 39l, (e) M16 2.5c 2.2t 2g 45l.

Regarding the four installation force tests, Table 3 presents the maximum forces recorded during these tests. All the maximum forces were found to be smaller than 1.0 kN, indicating that all the tested SCDBBs could be easily pushed through the bolt hole without the need for tools. By comparing the geometric features and dimensions of the EENs before and after the tests, negligible changes within the margin of error were observed, indicating that no plasticity had developed in the blades during installation.

Table 2 Results of tests.

Test type	Specimen	Failure mode	Ultimate resistance / Max force (kN)
Tensile loading tests	M8 2c 2.3t 1.7g 20l	Bolt shank fracture	40.74
	M8 2.5c 2.3t 1.5g 37l	Bolt shank fracture	42.65
	M8 2.7c 2.2t 1.8g 37l	Bolt shank fracture	41.84
	M12 3c 2t 2g 39l	Blade buckling	58.60
	M16 2.5c 2.2t 2g 45l	Blade buckling	152.14
Installation tests	M8 2.5c 2.3t 1.5g 37l	-	0.36
	M8 2.7c 2.2t 1.8g 37l	-	0.71
	M12 3c 2t 2g 39l	-	0.51
	M16 2.5c 2.2t 2g 45l	-	0.70

5. Numerical modelling and validation

In order to facilitate a more comprehensive numerical parametric study, a finite element (FE) modelling procedure was developed for SCDBBs. This procedure was validated by comparing the experimental test results with the numerical results, which will be elaborated in this section.

5.1. Finite element modelling method

Numerical models to simulate the tensile loading tests and installation tests were constructed in the commercial finite element software package ABAQUS 2019 [34]. For all components of the structure, the general-purpose 3-dimensional 8-noded solid elements of the type C3D8R were used. For modelling each SCDBB, individual components were initially created and then assembled to form the complete bolt, as depicted in Fig. 16. The threads in the bolt shank and nuts were not included in the model. However, in order to account for the reduction in cross-sectional area arising from the threads, the diameter of the bolt shank was adjusted to maintain the same net cross-sectional area as that of a real threaded bolt shank. The diameter of the nut hole was modified accordingly. The connection between the bolt shank and nuts was

modelled using the 'tie' constraint. Additionally, an out-of-straightness of the ratio 1/500 was introduced at the mid-span of the EEN blades to consider the imperfection due to fabrication tolerances. The material properties for each component were defined in accordance with the coupon test results. The plastic material behaviour was defined using the isotropic hardening rule. The material properties for the Grade 10.9 bolt shank were adopted from the reference [35].

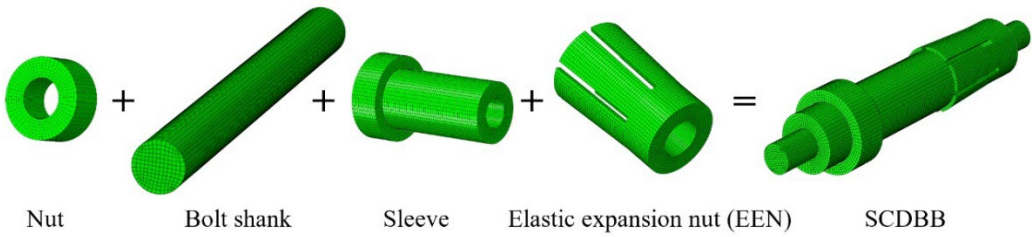

Fig. 16. FE models of SCDBB in parts and full assembly.

The test rigs were modelled and assembled to match the setup used in the experimental tests, as shown in Figs. 17 and 18. The test rigs and bolts were initially positioned so that the bolt shank and the bolt hole were in contact, which is a closer representation of the real condition. The 'hard contact' was employed to define the normal contact behaviour between steel components, and the frictional contact behaviour was defined for tangential contact. A static friction coefficient of 0.3 was assigned to surfaces without lubricating oil for tensile resistance tests [36], while a kinetic/sliding friction coefficient of 0.15 was used for lubricated surfaces in installation force tests [37].

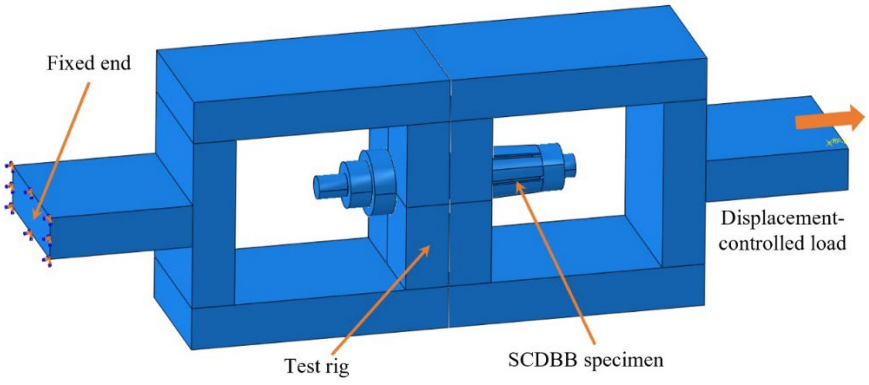

Fig. 17. FE model for tensile loading tests.

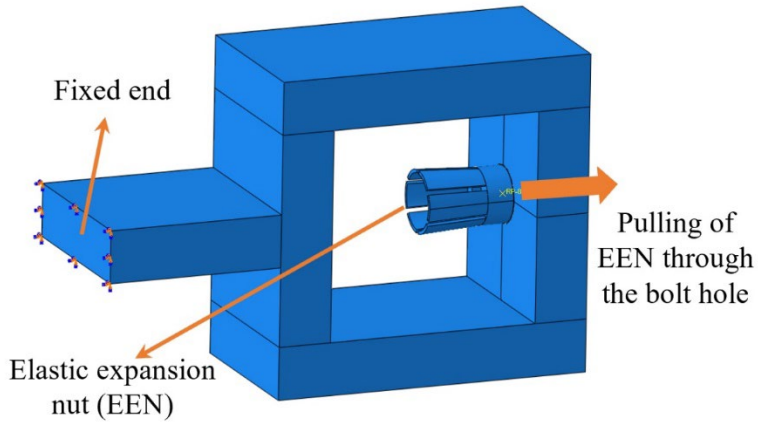

Fig. 18. FE model for installation tests.

For simulation of the tensile loading tests, one end of the test rig was fixed, and the load was applied to the other end. For simulation of the installation tests, the end of the test rig was fixed, and the load was applied to the end face of the EEN in order to draw the EEN through the bolt hole.

5.2.Mesh sensitivity study

The accuracy of numerical simulation results can be influenced by the mesh of finite element (FE) models, particularly for critical components [38–40]. Theoretical analyses and experimental tests have demonstrated the significant role of the EEN blades in the behaviour of SCDBBs under tensile loading and during the installation process. A key mesh parameter for the blades is the layer of elements through their thickness. In this study, the sensitivity to the mesh layers of elements of blades was studied. Numerical models were developed for the M12 and M16 specimens in the installation tests. For each EEN model, the layer of elements for the blades varied from 1 layer to 4 layers, as depicted in Fig. 19. Fig. 20 presents the comparison of results of the same model

with different layers of mesh. As shown, results converged with 3 layers, which will be adopted in the following FE models.

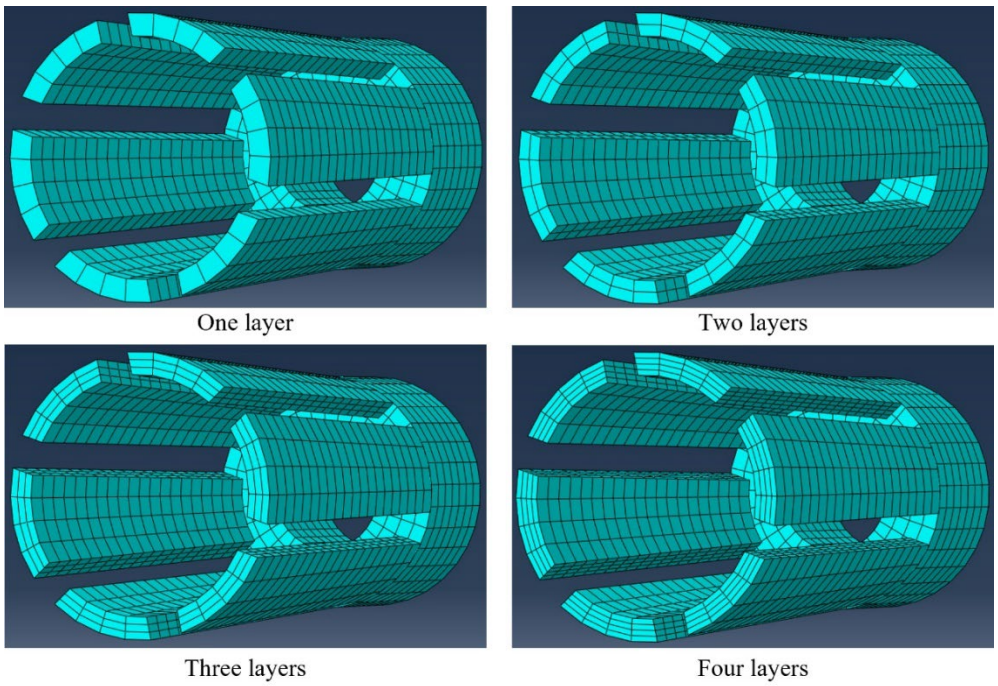

Fig. 19. Elastic expansion nut with different layers of mesh in blades.

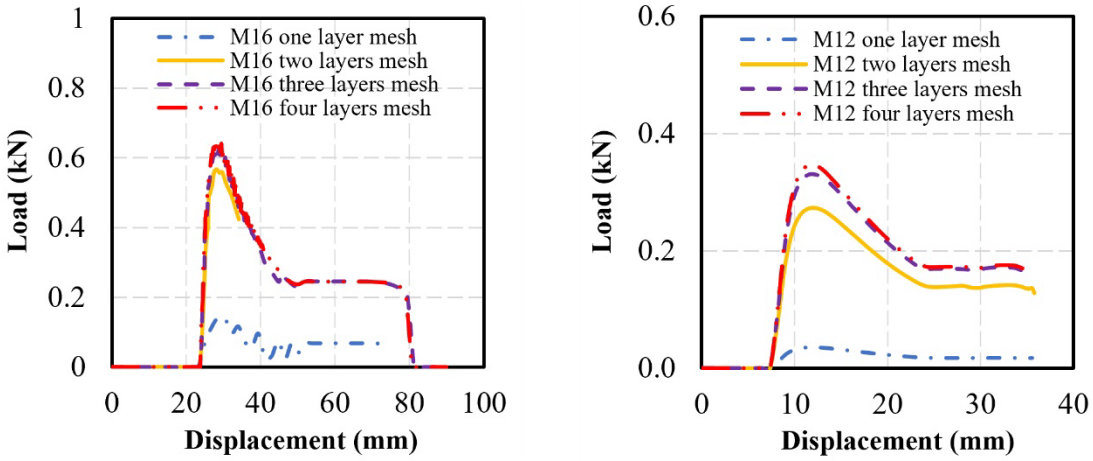

Fig. 20. Effect of different layers of mesh on installation forces.

5.3. Validation of the FE modelling method

To validate the developed FE modelling method, numerical simulations were conducted for all the tensile loading tests and the installation tests presented in Section

4. Comparison between the experimental test results and the numerical results was then performed. Firstly, for the five tensile loading tests, the FE simulations accurately captured the failure modes observed in the tests, as shown in Fig. 21. Furthermore, the ultimate resistances predicted by the FE simulations matched well with the corresponding test results. As shown in Table 4, the ratios of the FE result to the test result ranged from 0.93 to 1.1, with a mean of 0.99. Notably, there were slightly larger discrepancies observed for the two test specimens that experienced blade buckling, resulting in FE-to-test ratios of 0.93 and 1.1. This discrepancy can be attributed to the sensitivity of blade buckling to various factors, including imperfections, deviations from straightness, and flatness of the contact surfaces, etc. It is possible that these factors were not precisely captured in the FE models. However, overall, the developed FE models demonstrate a commendable ability to accurately represent the behaviour of SCDBBs under tensile loading.

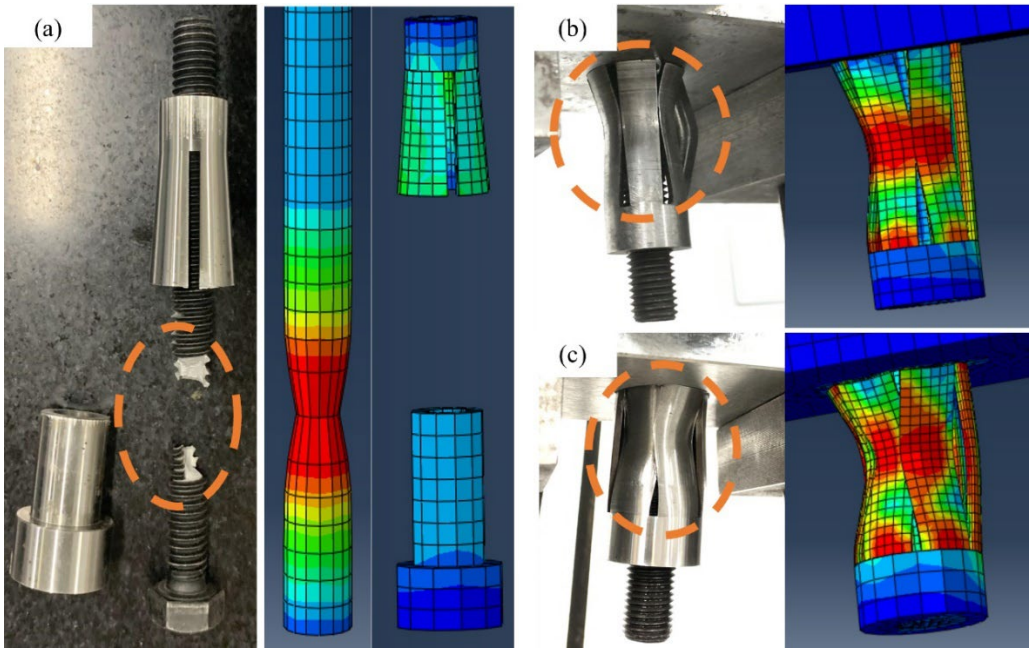

Fig. 21.Comparison between FE and test results: (a) fracture of bolt shank of M8 specimens, (b) blade buckling of specimen M12 3c 2t 2g 39l, (c) blade buckling of specimen M16 2.5c 2.2t 2g 45l.

Table 3 Comparison between test and FE results for the tensile loading tests

Specimen ID	Ultimate resistance (kN)			Failure mode	
	Test	FE	FE to Test Ratio	Test	FE
M8 2c 2.3t 1.7g 20l	40.74	40.7	1.0	Bolt shank fracture	Bolt shank fracture
M8 2.5c 2.3t 1.5g 37l	42.65	40.7	0.96	Bolt shank fracture	Bolt shank fracture
M8 2.7c 2.2t 1.8g 37l	41.84	40.7	0.97	Bolt shank fracture	Bolt shank fracture
M12 3c 2t 2g 39l	58.60	64.3	1.1	Blade buckling	Blade buckling
M16 2.5c 2.2t 2g 45l	152.14	141.0	0.93	Blade buckling	Blade buckling

Regarding the installation tests, the FE simulations predicted the maximum installation forces with satisfactory accuracy, as shown in Table 5. The discrepancy between the FE and test results was mainly attributed to the significant variation in the real frictional force. Additionally, the forces were measured by the built-in sensor of the 600 kN loading machine. Since the maximum forces were of small magnitude (all below 1 kN), the measurement errors may have had a considerable impact on the accuracy of the collected data. Moreover, the FE simulations predicted no plasticity, which aligned well with the experimental observations.

Overall, the developed FE modelling procedure was successfully validated to simulate the behaviour of SCDBBs under tensile loading and during installation with satisfactory accuracy. This lays the foundation for conducting more extensive numerical parametric studies.

Table 4 Comparison between test and FE results for the installation tests

Specimen ID	Max force (kN)		Plasticity	
	Test	FE	Test	FE
M8 2.5c 2.3t 1.5g 37l	0.36	0.22	None	None
M8 2.7c 2.2t 1.8g 37l	0.71	0.56	None	None
M12 3c 2t 2g 39l	0.51	0.33	None	None
M16 2.5c 2.2t 2g 45l	0.70	0.76	None	None

6. Parametric study

In order to analyse a wider range of design scenarios, understand the impact of key design parameters on behaviour, and optimise the design, a parametric study was conducted and detailed in this section.

6.1. Parametric analyses

The experimental tests highlighted the significance of the EEN blades in determining the behaviour of SCDBBs during installation and under tensile loading. Four key geometric parameters were identified for the blades: length (l), thickness (t), gap (g), and cut width (c). A reference design case was initially defined for each M8, M12, and M16 SCDBB by applying the constraints discussed in Section 3. To examine the influence of the four identified design parameters, variations were made to each parameter independently. This resulted in a total of 53 design cases, whose details are presented in Tables 6, 7, and 8, respectively. For each of the 53 design cases, two FE models were created and analysed to simulate the behaviour under tensile loading and during installation. Consequently, a total of 106 FE simulations were conducted, which form the basis for the discussion on the effect of the four design parameters in the subsequent sections. The nominal material properties were used for the FE models in the parametric study.

Table 5 Parametric design cases of M8 SCDBBs

Specimen Label	l (mm)	t (mm)	g (mm)	c (mm)
Reference case M8 2.4t 1.6g 3.0c 40l	40	2.4	1.6	3.0
M8 2.4t 1.6g 3.0c 30l	30	2.4	1.6	3.0
M8 2.4t 1.6g 3.0c 35l	35	2.4	1.6	3.0
M8 2.4t 1.6g 3.0c 45l	45	2.4	1.6	3.0
M8 2.4t 1.6g 3.0c 50l	50	2.4	1.6	3.0

M8 2.0t 1.6g 3.0c 40l	40	2.0	1.6	3.0
M8 2.2t 1.6g 3.0c 40l	40	2.2	1.6	3.0
M8 2.6t 1.6g 3.0c 40l	40	2.6	1.6	3.0
M8 2.8t 1.6g 3.0c 40l	40	2.8	1.6	3.0
M8 2.4t 1.2g 3.0c 40l	40	2.4	1.2	3.0
M8 2.4t 1.4g 3.0c 40l	40	2.4	1.4	3.0
M8 2.4t 1.8g 3.0c 40l	40	2.4	1.8	3.0
M8 2.4t 2.0g 3.0c 40l	40	2.4	2.0	3.0
M8 2.4t 1.6g 2.6c 40l	40	2.4	1.6	2.6
M8 2.4t 1.6g 2.8c 40l	40	2.4	1.6	2.8
M8 2.4t 1.6g 3.2c 40l	40	2.4	1.6	3.2
M8 2.4t 1.6g 3.4c 40l	40	2.4	1.6	3.4

Table 6 Parametric design cases of M12 SCDBBs

Specimen Label	l (mm)	t (mm)	g (mm)	c (mm)
Reference case M12 2.2t 2.2g 2.2c 45l	45	2.2	2.2	2.2
M12 2.2t 2.2g 2.2c 35l	35	2.2	2.2	2.2
M12 2.2t 2.2g 2.2c 40l	40	2.2	2.2	2.2
M12 2.2t 2.2g 2.2c 50l	50	2.2	2.2	2.2
M12 2.2t 2.2g 2.2c 55l	55	2.2	2.2	2.2
M12 1.8t 2.2g 2.2c 45l	45	1.8	2.2	2.2
M12 2.0t 2.2g 2.2c 45l	45	2.0	2.2	2.2
M12 2.4t 2.2g 2.2c 45l	45	2.4	2.2	2.2
M12 2.6t 2.2g 2.2c 45l	45	2.6	2.2	2.2
M12 2.2t 1.8g 2.2c 45l	45	2.2	1.8	2.2
M12 2.2t 2.0g 2.2c 45l	45	2.2	2.0	2.2
M12 2.2t 2.4g 2.2c 45l	45	2.2	2.4	2.2
M12 2.2t 2.6g 2.2c 45l	45	2.2	2.6	2.2
M12 2.2t 2.2g 1.8c 45l	45	2.2	2.2	1.8
M12 2.2t 2.2g 2.0c 45l	45	2.2	2.2	2.0
M12 2.2t 2.2g 2.4c 45l	45	2.2	2.2	2.4
M12 2.2t 2.2g 2.6c 45l	45	2.2	2.2	2.6

Table 7 Parametric design cases of M16 SCDBBs

Specimen Label	l (mm)	t (mm)	g (mm)	c (mm)
Reference case M16 2.4t 2.2g 2.4c 50l	50	2.4	2.2	2.4
M16 2.4t 2.2g 2.4c 40l	40	2.4	2.2	2.4
M16 2.4t 2.2g 2.4c 45l	45	2.4	2.2	2.4
M16 2.4t 2.2g 2.4c 55l	55	2.4	2.2	2.4

M16 2.4t 2.2g 2.4c 60l	60	2.4	2.2	2.4
M16 2.4t 2.2g 2.4c 65l	65	2.4	2.2	2.4
M16 2.4t 2.2g 2.4c 70l	70	2.4	2.2	2.4
M16 2.0t 2.2g 2.4c 50l	50	2.0	2.2	2.4
M16 2.2t 2.2g 2.4c 50l	50	2.2	2.2	2.4
M16 2.6t 2.2g 2.4c 50l	50	2.6	2.2	2.4
M16 2.8t 2.2g 2.4c 50l	50	2.8	2.2	2.4
M16 2.4t 1.8g 2.4c 50l	50	2.4	1.8	2.4
M16 2.4t 2.0g 2.4c 50l	50	2.4	2.0	2.4
M16 2.4t 2.4g 2.4c 50l	50	2.4	2.4	2.4
M16 2.4t 2.6g 2.4c 50l	50	2.4	2.6	2.4
M16 2.4t 2.2g 2.0c 50l	50	2.4	2.2	2.0
M16 2.4t 2.2g 2.2c 50l	50	2.4	2.2	2.2
M16 2.4t 2.2g 2.6c 50l	50	2.4	2.2	2.6
M16 2.4t 2.2g 2.8c 50l	50	2.4	2.2	2.8

6.2. Effect of length

Fig. 22(a) illustrates the relationship between the ultimate resistance of SCDBB under tensile loading and the length of the EEN blades. The graph demonstrates that as the length of the blades increases, the failure mode changes from fracture of the bolt shank to buckling of the EEN blades. This observation aligns with the theoretical prediction outlined in Section 3.4.

Fig. 22(b) depicts the changes in the maximum installation force and the development of plasticity in the blades as the length of the blades varies. The graph illustrates that with the increase in the blade length, the maximum installation forces reduce at a decreasing rate. This decrease occurs because longer blades have less bending stiffness, leading to lower contact forces between the blades and the bolt hole during installation. Consequently, a reduced frictional force is generated. It is worth noting that as the blade length shortens and stiffness increases, plasticity may occur at the blade root. This plastic deformation remains even after the blades pass through the bolt hole.

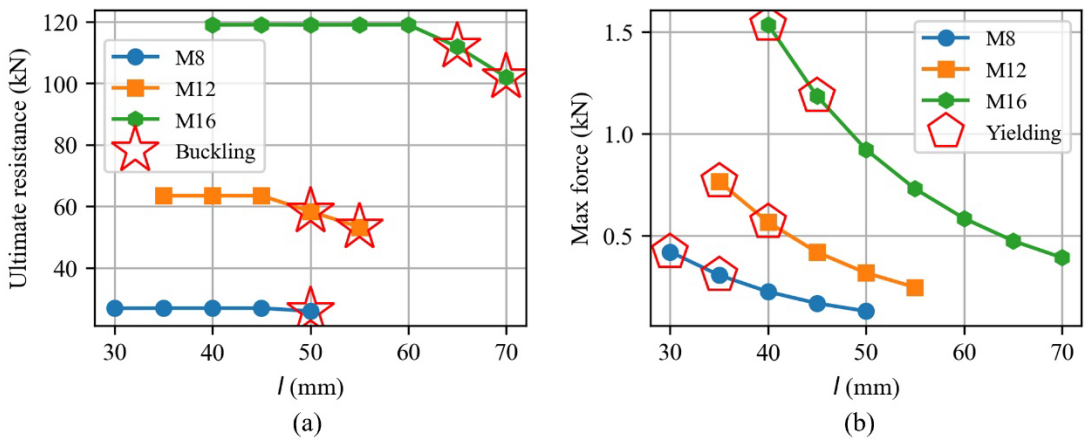

Fig. 22.Effect of the length of blades: (a) under tensile loading, (b) during installation.

While reducing the length of the blades effectively avoids buckling, it also leads to higher installation forces. Additionally, shorter blades may introduce plasticity at the blade root, causing the blades to not return to their original positions and potentially resulting in insufficient contact between the blades and the connected components. Therefore, careful consideration must be given to selecting the blade length, balancing its behaviour under tensile loading and during installation. Based on the parametric analyses, the appropriate ranges for blade length variations are (35, 45), (35, 45), and (45, 55) mm for the reference cases of M8, M12, and M16, respectively.

6.3.Effect of thickness

Fig. 23(a) depicts the relationship between the ultimate resistance of SCDBB under tensile loading and the thickness of blades. As the thickness increases, the blades become relatively stronger compared to the bolt shank. The failure mode remains consistent, with the bolt shank fracturing and the ultimate resistance of the bolt remaining unchanged. However, when the thickness of the blades decreases, there is a potential for blade buckling to occur, resulting in decreased ultimate resistance.

In Fig. 23(b), the maximum installation force and the development of plasticity in the blades are shown in relation to the thickness of blades. For all three bolt sizes, the

maximum installation forces increase nearly linearly with the increase in blade thickness. Additionally, no plasticity is observed at the blade root for the various blade thicknesses studied. This suggests that the blades will return to their original positions after being pushed through the bolt hole.

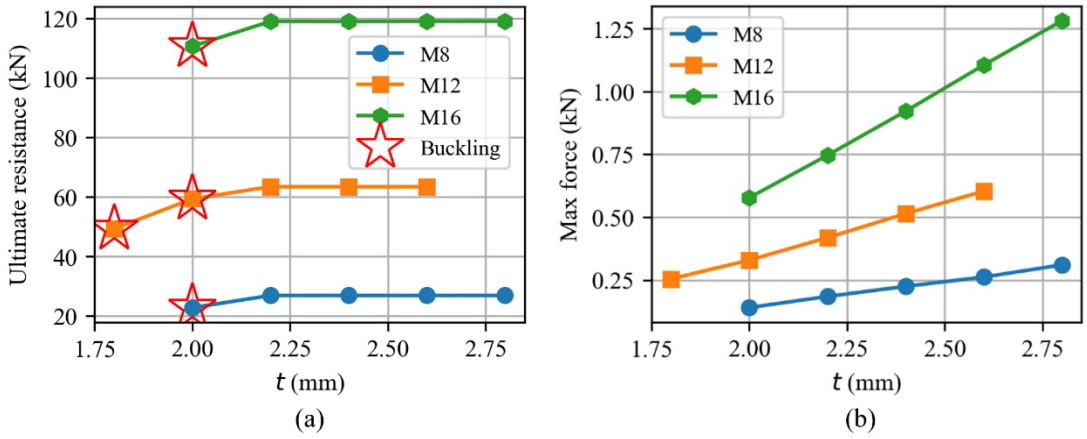

Fig. 23. Effect of the thickness of blades: (a) under tensile loading, (b) during installation.

Increasing the thickness of the blades effectively enhances their resistances. To prevent buckling, the thickness should be greater than 2.2 mm for the three reference cases of M8, M12, and M16. The variation in thickness does not cause plasticity during the installation process, but the upper bound of thickness should consider the increased installation force, as it may make installation more difficult.

6.4.Effect of gap

Fig. 24(a) illustrates the variation of ultimate resistance of SCDBB under tensile loading with the gap of blades. In general, the variation in the gap of blades does not result in variation in the ultimate resistance under tensile loading, as it does not result in notable variation in the resistance of blades and therefore does not lead to change of failure modes. However, for the M12 1.8g and M16 1.8g cases, where the gaps are

small and the blade end faces do not fully contact the connected plate, the blades experienced eccentric compression and buckled before the bolt shanks developed their full resistance.

In Fig. 24(b), the maximum installation force and the development of plasticity in the blades are shown in relation to the gap of blades. The maximum installation forces increase linearly with the increase in the gap, as larger gaps require more compression of the blades to pass through the bolt hole. It is also observed that for M8 cases with a gap larger than 1.8 mm, M12 cases with a gap larger than 2.4 mm, and M16 cases with a gap larger than 2.4 mm, plasticity develops at the blade root during installation.

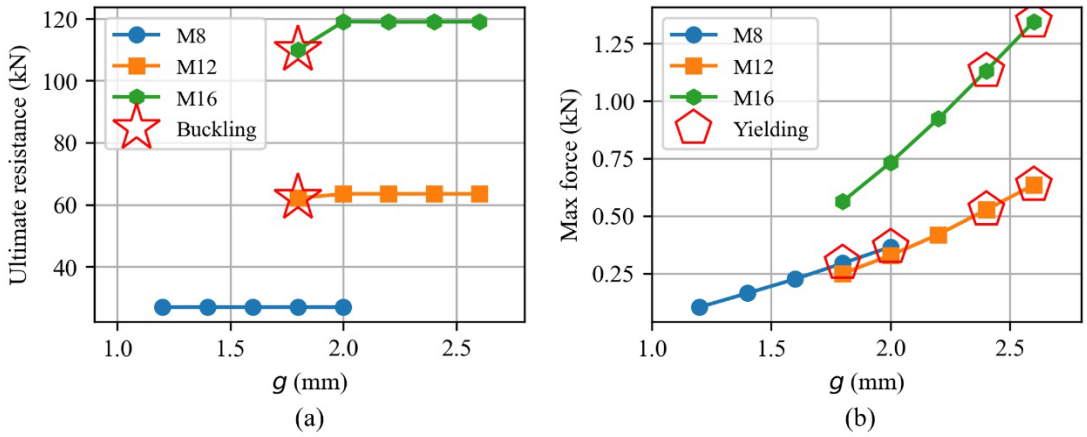

Fig. 24. Effect of the gap of blades: (a) under tensile loading, (b) during installation.

To achieve a balance between behaviour under tensile loading and installation, the gap of blades should be carefully designed. A small gap may result in partial contact between the blades and the connected component, leading to eccentric compression and buckling under tensile loading. On the other hand, a large gap requires significant installation force and may induce plasticity at the blade root during installation. Based on the parametric analyses, the appropriate blade gaps for the reference cases of M8, M12, and M16 should fall within the ranges of (1.2, 1.6), (2.0, 2.2), and (2.0, 2.2) mm, respectively.

6.5.Effect of cut width

Fig. 25(a) shows the variation of ultimate resistance of SCDBB under tensile loading with the cut width of blades. It can be observed that the ultimate resistances remain unchanged, and the failure mode remains the same (i.e., bolt shank fracture) for the different cut widths studied. As the cut width increases, the maximum installation force decreases (as shown in Fig. 25(b)) due to less blade area. However, the reduction is minimal.

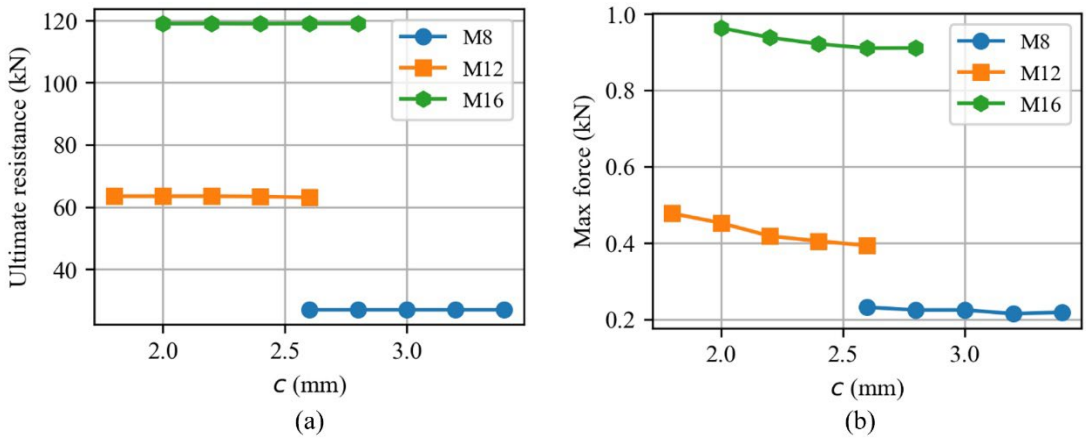

Fig. 25. Effect of the cut width of blades: (a) under tensile loading, (b) during installation.

As can be seen, the behaviour of SCDBBs shows limited sensitivity to the cut width. Given the only geometric constraint of the cut width is to avoid conflict between blades during the installation process, as elaborated in Section 3.1. The implication for design is that during design process, the cut width can be firstly determined to speed up the optimisation process.

6.6. Validation of analytical models

The analytical models presented in Section 3 serve as a preliminary means of determining the geometric dimensions of the bolts and act as a starting point for further

optimisation. Based on these models, geometric dimension constraints were derived to prevent blade buckling under tensile loading and blade yielding during installation. To assess their accuracy, comparison was conducted between the predictions from the analytical models and the results obtained in experimental tests with the reference cases in FE simulations. The comparison is summarized in Table 9.

As depicted in Table 9, the predictions from the analytical models align well with the experimental and FE results in the majority of cases. This strong correlation serves as validation for the accuracy of the analytical models. Therefore, the theoretical models presented in Section 3 can be regarded as reliable tools for preliminary determination of SCDBB dimensions.

Table 9 Comparison between analytical predictions and results of experimental tests and FE simulations

	Specimen label	Failure mode		Yielding of blades	
		Prediction	Result	Prediction	Result
Test	M8 2c 2.3t 1.7g 20l	Bolt shank fracture	Bolt shank fracture	Y	Y
	M8 2.5c 2.3t 1.5g 37l	Bolt shank fracture	Bolt shank fracture	N	N
	M8 2.7c 2.2t 1.8g 37l	Bolt shank fracture	Bolt shank fracture	N	N
	M12 3c 2t 2g 39l	Blade buckling	Blade buckling	N	N
	M16 2.5c 2.2t 2g 45l	Blade buckling	Blade buckling	N	N
FE	M8 2.4t 1.6g 3.0c 40l	Bolt shank fracture	Bolt shank fracture	N	N
	M12 2.2t 2.2g 2.2c 45l	Blade buckling	Bolt shank fracture	N	N
	M16 2.4t 2.2g 2.4c 50l	Blade buckling	Bolt shank fracture	N	N

7.Conclusions and design recommendations

A novel blind bolt, that combines high tensile resistance and stiffness with easy and fast installation/demounting capabilities, was proposed in this study and named SCDBB (Swift-Constructed Demountable Blind Bolt). The components, intended working mechanism, and fabrication process of SCDBBs were introduced. Geometric constraints of the critical components were then derived based on the desired behaviour. To study the behaviour of SCDBBs under tensile loading and performance during

installation process, 9 experimental tests were conducted. Subsequently, numerical finite element (FE) models are developed and validated by comparing the numerical results with the experimental data. To further explore the impact of key design parameters on the behaviour of the bolts under tensile loading and during installation, parametric studies consisting of 106 FE models were conducted for bolts of three sizes with variations in four key design parameters. The main findings and conclusions are as follows.

1. The proposed SCDBBs can be installed and removed in a fast and efficient manner, which has been verified by the practice of 9 experimental tests. For the studied bolts of 3 different sizes (M8, M12, and M16), the maximum installation forces are generally less than 1 kN.

2. Under maximum tensile loading, two failure modes, namely, the fracture of bolt shank and the buckling of the EEN blades, are revealed. The former is preferred as the buckling of the EEN blades will alter the force transferring mechanism and result in an abrupt loss in the bolt resistance.

3. Reducing the length of the blades can effectively prevent buckling. However, shorter blades will lead to higher installation forces. Additionally, shorter blades may introduce plasticity at the blade root, causing the blades to not return to their original position and potentially resulting in insufficient contact between the blades and the connected components. Careful consideration must be given to selecting the blade length, balancing its behaviour under tensile loading and during installation. The appropriate range for blade length variations is (35, 45), (35, 45), and (45, 55) mm for the reference cases of M8, M12, and M16, respectively.

4. Increasing the thickness of the blades can effectively enhance their resistances, and to prevent buckling, the thickness should be greater than 2.2 mm for the three reference

cases of M8, M12, and M16. The variations in thickness in the parametric study did not cause plasticity during the installation process, but the upper limit of thickness should consider the increased installation force, as it may make installation more difficult.

5. A small gap may result in partial contact between the blades and the connected component, leading to eccentric compression and buckling under tensile loading. On the other hand, a large gap requires significant installation force and may induce plasticity at the blade root during installation. Based on the parametric analyses, the appropriate blade gaps for the reference cases of M8, M12, and M16 should fall within the ranges of (1.2, 1.6), (2.0, 2.2), and (2.0, 2.2) mm, respectively.

6. The behaviour of SCDBBs is less sensitive to the cut width of the EEN blades. To speed up the optimisation process, the cut width can be firstly determined based on the geometric constraint to avoid conflict between blades during the installation process.

CRediT authorship contribution statement

Xiao-Zhou Han: Conceptualization, Methodology, Visualization, Investigation, Writing – original draft. **Chen Wang:** Visualization, Investigation, Supervision, Writing – original draft, Writing – review & editing. **Tak-Ming Chan:** Conceptualization, Methodology, Supervision, Writing – review & editing.

Declaration of Competing Interest

The authors declare that they have no known competing financial interests or personal relationships that could have appeared to influence the work reported in this paper.

Data availability

Data will be made available on request.

Acknowledgments

The authors sincerely acknowledge the support received from the Chinese National Engineering Research Centre for Steel Construction (Hong Kong Branch) at The Hong Kong Polytechnic University. The authors would also like to thank Mr. Long Liang for his assistance during the experiments. The help from Dr. Juncai Liu and Mr. Meng Yang from Shandong University on coding is gratefully acknowledged.

References

[1] Y. Kurobane, J.A. Packer, J. Wardenier, N. Yeomans, Design Guide for Structural Hollow Section Column Connections. CIDECT Design Guide No. 9, TÜV-Verlag, K¨oln, 2004.

[2] Lindapter, Hollo-bolt, 2023, https://www.lindapter.com/ (Accessed 13/09/2023).

[3] Blindbolt, Thin Wall Bolt, 2023, https://www.blindbolt.com/thin-wall-bolt/ (Accessed 13/09/2023).

[4] AJAX Fasteners, Oneside Bolt, 2023, https://www.icc-nta.org/newsmedia/press-release/ajax/ (Accessed 13/09/2023).

[5] AJAX Fasteners, Oneside Hi-shear Bolt, 2023, https://www.icc-nta.org/newsmedia/press-release/ajax/ (Accessed 13/09/2023).

[6] Huck, Huck Blind Fasteners, 2023, https://www.hfsindustrial.com/selector/bom.html (Accessed 13/09/2023).

[7] Blindbolt, Blind Bolt, 2023, https://www.blindbolt.com/the-blind-bolt/ (Accessed 13/09/2023).

[8] Blindbolt, Heavy Duty Bolt, 2023, https://www.blindbolt.com/heavy-duty-bolt/ (Accessed 13/09/2023).

[9] Aerobolt, Jack Nut, 2023, https://huckaerobolt.com.au/blogs/news/what-is-a-nutsert (Accessed 13/09/2023).

[10] H.Y. Loh, B. Uy, M.A. Bradford, The effects of partial shear connection in composite flush end plate joints part I—experimental study, J. Constr. Steel Res. 62 (4) (2006) 378–390.

[11] A.Y. Elghazouli, C. M´alaga-Chuquitaype, J.M. Castro, A.H. Orton, Experimental monotonic and cyclic behaviour of blind-bolted angle connections, Eng. Struct. 31 (11) (2009) 2540–2553.

[12] J.F. Wang, L.H. Han, B. Uy, Hysteretic behaviour of flush end plate joints to concrete-filled steel tubular columns, J. Constr. Steel Res. 65 (8–9) (2009) 1644–1663.

[13] Z.Y. Wang, W. Tizani, Q.Y. Wang, Strength and initial stiffness of a blind-bolt connection based on the T-stub model, Eng. Struct. 32 (9) (2010) 2505–2517.

[14] J. Wang, B.F. Spencer Jr., Experimental and analytical behaviour of blind bolted moment connections, J. Constr. Steel Res. 82 (2013) 33–47.

[15] D. Li, B. Uy, F. Aslani, V. Patel, Behaviour and design of demountable CFST column-column connections under tension, J. Constr. Steel Res. 138 (2017) 761–773.

[16] W. Wang, L. Li, D. Chen, T. Xu, Progressive collapse behaviour of extended endplate connection to square hollow column via blind hollo-bolts, Thin-Walled Struct. 131 (2018) 681–694.

[17] W. Tizani, A. Al-Mughairi, J.S. Owen, T. Pitrakkos, Rotational stiffness of a blind-bolted connection to concrete-filled tubes using modified hollo-bolt, J. Constr. Steel Res. 80 (2013) 317–331.

[18] M. Cabrera, W. Tizani, J. Ninic, F. Wang, Experimental and numerical analysis of preload in extended hollo-bolt blind bolts, J. Constr. Steel Res. 186 (2021), 106885.

[19] P.P. Debnath, T.M. Chan, Experimental performance of single blind bolted CFST column connection under predominant shear loading, J. Constr. Steel Res. 196 (2022), 107386.

[20] P.P. Debnath, T.M. Chan, Experimental evaluation and component model for single anchored blind-bolted concrete filled tube connections under direct tension, J. Constr. Steel Res. 196 (2022), 107391.

[21] W. Tizani, D.J. Ridley-Ellis, The performance of a new blind-bolt for moment-resisting connections, in: Tubular Structures X, Routledge, 2003, pp. 395–400.

[22] T.C. Barnett, W. Tizani, D.A. Nethercot, Development of a blind bolting system, in: Proceedings of the International Conference on Steel Structures of the 2000's, 11th-13th September, 2000 September, pp. 65–70.

[23] X.Z. Han, T.M. Chan, A swift-constructed elastic expansion nut and demountable blind bolt, in: Patent No. ZL202220239181.3, Utility Model Patent, China National Intellectual Property Admin-istration, The Government of People's Republic of China, 2022.

[24] X.Z. Han, T.M. Chan, Tensile, shear, and slip-resistance behaviours of swift-constructed demountable blind bolt, 2024. In preparation for submission.

[25] X.Z. Han, T.M. Chan, Auxiliary installation tool for blind bolt, in: Patent No. ZL202223211533.3, Utility Model Patent, China National Intellectual Property Administration, The Government of People's Republic of China, 2023.

[26] G.Q. Li, Blind bolting for connections between H-shaped beam and rectangular hollow section column, in: HKIE Structural Division Annual Seminar, 2021.

[27] J.L. Quan, Analysis of the reasons for bolt head damage of 40Cr steel bolts and improvement of heat treatment process, Metal Processing (Heat Processing) 03 (2010) 37–38.

[28] G.F. Sun, Fracture analysis of 40Cr steel bolts, Metal Products 37 (05) (2011) 80–82.

[29] GB/T 3077-2015, Chinese Code: Alloy Structure Steels, Beijing, China, 2015 (In Chinese).

[30] X.Z. Han, T.M. Chan, Swift-Constructed Demountable Blind Bolt for Fast Execution and Disassembling of SHS Connection. Proceedings of the 10th European Conference on Steel and Composite Structures - EUROSTEEL 2023, ce/papers, 6(3-4), pp.428-433.

[31] GB/T 3098.1–-2010, Code for Mechanical Properties of Fasteners-Bolts, Screws, and Studs, Standards Press of China, Beijing, 2010 (In Chinese).

[32] ISO 898–- 1:2013, Mechanical Properties of Fasteners Made of Carbon Steel and Alloy Steel - Part 1: Bolts, Screws, and Studs with Specified Property Classes - Coarse Thread and Fine Pitch Thread, 2013.

[33] EN 14399-3: 2015, High-Strength Structural Bolting Assemblies for Preloading–Part 3: System HR–Hexagon Bolt and Nut Assemblies, 2015.

[34] ABAQUS, ABAQUS 2020, Dassault Syst`emes Simulia Corp, Providence, RI, 2019.

[35] X. Gao, W. Wang, L.H. Teh, L. Zhuang, A novel slip-critical blind bolt: experimental studies on shear, tensile and combined tensile–shear resistances, Thin-Walled Struct. 170 (2022), 108630.

[36] R.J.M. Pijpers, H.M. Slot, Friction coefficients for steel-to-steel contact surfaces in air and seawater, J. Phys. Conf. Ser. 1669 (1) (2020) 012002. IOP Publishing.

[37] R.T. Barrett, Fastener Design Manual (No. NAS 1.61: 1228), 1990.

[38] P.P. Debnath, T.M. Chan, A comprehensive numerical approach for modelling blind bolted CFST connections, in: Structures vol. 33, Elsevier, 2021, pp. 2208–2225.

[39] C. Wang, A. Rudman, R. Tremblay, C.A. Rogers, Numerical investigation into I-shape brace connections of conventional concentrically braced frames, Eng. Struct. 236 (2021), 112091.

[40] C. Wang, R. Tremblay, C.A. Rogers, Parametric study on the I-shape brace connection of conventional concentrically braced frames, J. Constr. Steel Res. 182 (2021), 106669.